

Article

# Investigation of Pressure Chambers for Integrated Fluidic Actuators in Adaptive Slabs <sup>†</sup>

Matthias J. Bosch <sup>1,\*</sup>, Markus Nitzlader <sup>2</sup>, Matthias Bachmann <sup>1</sup>, Hansgeorg Binz <sup>1</sup>, Lucio Blandini <sup>2</sup>  
and Matthias Kreimeyer <sup>1,\*</sup>

<sup>1</sup> Institute for Engineering Design and Industrial Design (IKTD), University of Stuttgart, Pfaffenwaldring 9, 70569 Stuttgart, Germany

<sup>2</sup> Institute for Lightweight Structures and Conceptual Design (ILEK), University of Stuttgart, Pfaffenwaldring 14, 70569 Stuttgart, Germany

\* Correspondence: matthias.bosch@iktd.uni-stuttgart.de (M.J.B.); matthias.kreimeyer@iktd.uni-stuttgart.de (M.K.)

<sup>†</sup> This paper is an extended version of our published paper Bosch, M.J.; Nitzlader, M.; Bachmann, M.; Binz, H.; Blandini, L.; Kreimeyer, M. Experimental Testing of Actuator Chambers of Integrated Fluidic Actuators for Adaptive Slabs. In Proceedings of the ICEM20 20th International Conference on Experimental Mechanics, Porto, Portugal, 2–7 July 2023. Available online: [https://paginas.fe.up.pt/~icem20/proceedings\\_icem20/](https://paginas.fe.up.pt/~icem20/proceedings_icem20/) (accessed on 7 December 2023).

**Abstract:** A high proportion of the CO<sub>2</sub> emissions worldwide are caused by the construction sector or are associated with buildings. Every part of the industry needs to reduce its share of emissions, so the building sector must also do its part. One possible solution for achieving this reduction in the field of load-bearing structures is the use of adaptive structures. This research focuses on adaptive slab structures, which require specific actuators to be integrated into the system. Conventional actuators are not suitable due to the prevailing requirements, namely installation space and performance. For this investigation, the actuator is divided into different functional components. A rough description of the requirements for one component, namely the energy converter, is given. Different concepts are developed, tested, and compared with numerical results. Due to the requirements, the concepts are limited to hydraulics. The authors then present a comparison of different simulation strategies for the energy converter. Overall, this paper provides a new contribution to the design of energy converter concepts for integrated hydraulic actuators in slabs, along with experimental verification of the working principle of the energy converters to meet the requirements. A simplified numerical model is proposed to estimate the behavior of the energy converter during the early design phase.

**Keywords:** experimental testing; lightweight structures; slabs; fluid actuators; adaptivity; hydraulic; eco-sustainability



**Citation:** Bosch, M.J.; Nitzlader, M.; Bachmann, M.; Binz, H.; Blandini, L.; Kreimeyer, M. Investigation of Pressure Chambers for Integrated Fluidic Actuators in Adaptive Slabs. *Actuators* **2024**, *13*, 41. <https://doi.org/10.3390/act13010041>

Academic Editor: Luigi de Luca

Received: 8 December 2023

Revised: 8 January 2024

Accepted: 17 January 2024

Published: 19 January 2024



**Copyright:** © 2024 by the authors. Licensee MDPI, Basel, Switzerland. This article is an open access article distributed under the terms and conditions of the Creative Commons Attribution (CC BY) license (<https://creativecommons.org/licenses/by/4.0/>).

## 1. Introduction

### 1.1. Motivation

The construction sector is responsible for a high share of worldwide carbon dioxide emissions, with the cement in concrete structures having a particular impact [1].

One approach for reducing the mass of load-bearing structures is to make them adaptive, allowing them to react to external loads and reduce stresses and deformations. In this way, the structure can be built with less material [2]. Several studies [3,4] have demonstrated the potential for material and energy savings.

Actuation and actuator concepts for structural elements subjected to bending stress are investigated in the “Integrated fluidic actuators” sub-project at the Collaborative Research Centre 1244 (Sobek et al., 2021). An actuation principle for adapting deflection has been proved for beams in [5] with reference to a large-scale beam. Subsequent work has extended the investigations to address slabs. Since slabs are typically the structural element where

most resources are needed in buildings [6–8], this is expected to impact global warming potential significantly. Due to the multiaxial load transfer of slabs, new actuators and actuation principles are necessary. Actuators fulfilling the specific requirements of two-way slabs do not exist.

### 1.2. Previous Work

Adaptive structures offer the possibility of saving resources in the construction of future buildings. For this purpose, structural elements of buildings are therefore combined with actuators, sensors, and a control unit to enable a response to external loads [2].

An actuator has different sub-components, e.g., based on the logic of [9–11], which are addressed separately (cf. Figure 1):

- Energy provider, which provides non-mechanical energy in a controlled manner,
- Energy converter, which converts the non-mechanical energy into mechanical energy,
- Energy transmission, where energy is transferred to the desired location and applied to the surrounding system.

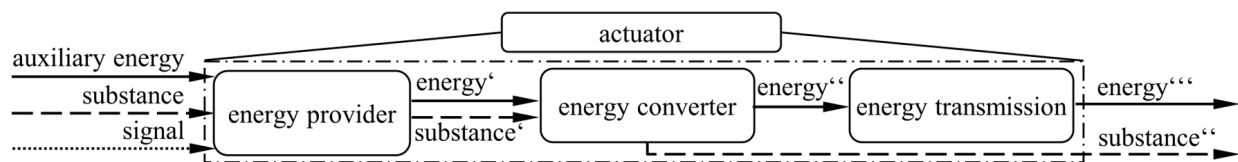


**Figure 1.** Simplified functional components of an actuator, based on the logic of [9–11]. The connecting flows are shown, with the hyphens marking the change of the flow variable due to the functional component. This can be, e.g., the conversion of hydraulic to mechanical energy.

Efforts to identify a solution to each of these components of actuators for slabs are ongoing in different investigations by the authors.

Research on adaptive civil structures dates back several decades [12]; however, adaptive structures are still rare in the built environment. Research is being undertaken at the University of Stuttgart as part of the Collaborative Research Center SFB 1244 [13]. A demonstration high-rise tower known as D1244 was built for this purpose as an example of an actuated truss structure. Further research deals with prestressed concrete beams [14] and the actuation of shells [15] using state-of-the-art actuators specially adapted to the task. In [16], a new actuator concept is used to actuate a concrete column.

Considerations relating to the minimization of the lifespan energy in the design process of adaptive structures have been outlined by Senatore et al. [17,18]. Two different prototypes were developed within the scope of this research: an actuated cantilever truss [19] and a pedestrian bridge with simple support [20]. Standard electromechanical actuators were used for these prototypes due to relatively low loads and, therefore, low necessary actuator forces.

Further research with a focus on structure control, actuation concepts, and actuator placement can be found for multi-story buildings [21–25], and also for shells [26], ribbed-stiffened slabs [27], bridges [28,29], shear walls [30] and truss structures [31]. Standardized actuators that are available on the market have been used when a realization has taken place.

Specific actuator concepts for integration into concrete structural elements have been developed and investigated by Kelleter and Burghardt [32], leading to a full-scale prototype of an adaptive beam [5]. An actuator is integrated outside the neutral fiber into the beam's cross-section. When activating the actuator, a force is generated, and a moment results due to the eccentricity, counteracting imposed bending moments (cf. Figure 2). As a result, the deflection caused by an external load can be reduced and even completely compensated. This work forms the basis of the investigation in this paper. The concepts for beams are transferred to biaxial spanning structural elements like concrete slabs.

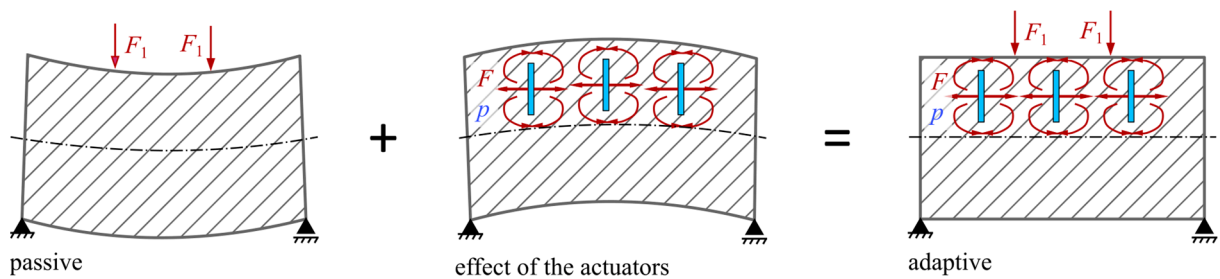


**Figure 2.** Illustration of an actuation concept for beams:  $F$  is the actuation force due to fluidic pressure  $p$  generated by the actuator applied on the structural element, the force flow around the actuators is shown with red arrows,  $F_1$  is the force due to external load on the structural element; cf. [33].

In different investigations, Nitzlader et al. [6] show actuation concepts for slabs, while Bosch et al. [34] show insight into the development of concepts for the energy transmission structure. Figure 3 shows the principal actuation concept used for the investigation.

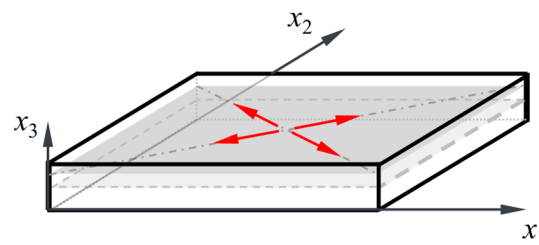


**Figure 3.** Example actuation concepts for a slab, with the red arrows symbolizing actuation forces inside the slab. The actuation force is the force generated by the actuator applied on the slab; cf. [34].

### 1.3. Main Contribution

This contribution focuses on one functional component of the actuator, namely the energy converter for the conversion of hydraulic energy to mechanical energy. Therefore, a new design concept is developed to meet the specific requirements of the slabs, as there are no actuators available yet that allow the material reduction of the slabs in the following steps. The focus is on the forces and strokes in the concepts and the investigation of simple numerical models for the later design of the complete actuator. Three concepts have been established and undergo experimental and numerical investigation. This paper is an expanded and revised version of the extended conference paper for the ICEM 2023 conference [33]. It offers a new contribution in:

1. Design and first physical setup of energy converters based on the identified requirements for adaptive slabs.
2. Validation of simplified numerical models for use in designing actuator concepts in the early design phase to estimate the behavior of the energy converter for different construction sizes.
3. Experimental validation of the performance of the energy converters to meet the identified requirements.

In extension to the extended conference paper, the following parts are new:

- The identification of two requirements, forces and stroke, within a specific construction space is deepened.
- The design discussion has been expanded, and new variants for future investigation have been proposed.
- The study of different modeling approaches for 2D, 3D, and material modeling has been added.

- The sensitivity of different parameters on the numerical models compared to the experimental results has been evaluated. In particular, a study of the influence of rotational deviations with a 3D-modelled simulation model has been added.

1.4. Structure of the Paper

First, the prototype design is presented. Therefore, the authors first define three concept classes based on a different conference contribution. This is followed by the identification of requirements, which forms the base for the design considerations in the following section. Afterward, the experimental setup and the numerical models for the verification and validation are presented. Finally, the results are presented and subsequently discussed.

2. Prototype Design

2.1. Basic Concepts for Integrated Actuators for Slabs

A previous conference publication of the authors has focused on the energy transmission structure for integrated actuators [34]. Therefore, the basic concept for the actuators has been classified into three concept classes, as seen in Table 1. The classification criteria were the effective range of the applied forces and the location of the energy converter in the actuator structure.

**Table 1.** Classification of actuator concepts according to [34], with black parts denoting the energy transmission structure and blue parts denoting the energy converter.  $F$  is the actuation force generated by the actuator applied on the slab,  $h$  is the lever arm regarding the neutral fiber of the structural element,  $M$  is the generated moment by  $F$  and the lever arm  $h$ .

Location Energy Converter	Central		Decentral
Effective Range	Local	Semi-Local	
Concept Class	CC1	CC2	CC3

In concept class one (CC1), the surfaces applying force are next to each other and coincide with the energy converter. The force in concept classes two and three is directed to specific locations, allowing the actuator to induce a constant moment  $M$  over a longer distance than CC1. This means the actuators of CC2 and CC3 operate in a semi-local manner. The differentiation of concept classes two (CC2) and three (CC3) is followed by the location of the energy converter. In CC2, the energy conversion occurs centrally at one point of the actuator, while in CC3, the conversion occurs at different locations.

Due to the available construction space and the necessary reduction in the number of actuators, CC3 appears to be the most promising concept class. The actuator needs to have defined contact points to the slab, with everything else needing to be separated using an enclosure or a separation medium [34].

Figure 4 features an example concept of an actuator with two actuated directions. The marked blue parts are filled and pressurized with a hydraulic fluid, generating a force. The forces are just applied on the structural element at the four outer sides of the actuator. The

counterforces of the hydraulic chambers are connected internally to the actuator via the energy transmission. In the following, just the energy converters in general are investigated (cf. Figure 4, orange marking).

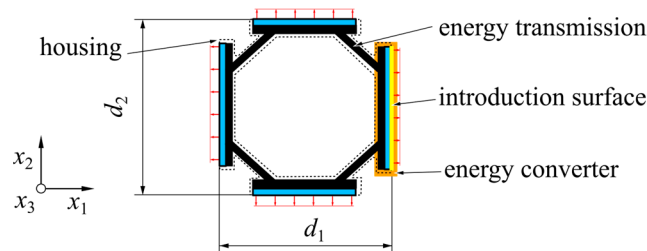


**Figure 4.** Schematic example actuator with different components. The investigated energy converter is marked in orange, the introduction surface is shown in yellow, the red arrows visualize the force generated by the actuator applied on the structural element. The main spatial directions are named  $x_1$ ,  $x_2$  and  $x_3$ ; cf. [33].

## 2.2. Requirements for Actuator Energy Converters for Adaptive Slabs

Different requirements for an actuator concept can be derived based on the work of Nitzlader et al. [6]. The most essential requirements are the expected construction space as well as the necessary force and stroke. In the case study [6], with a slab size of  $2\text{ m} \times 2\text{ m}$ , a slab height of 100 mm is preferred. This results in a maximum installation height for the actuator of around 45–50 mm (spatial direction  $x_3$  in Figure 4). For the outer edge dimensions (spatial directions  $x_1$  and  $x_2$ ), a square design with  $d_1 = 130\text{ mm}$  and  $d_2 = 130\text{ mm}$  is used. Even higher edge dimensions are possible and necessary for further concepts to limit the necessary number of actuators in one slab. For this investigation, the smallest dimension is assumed to reach the limits of the concepts and handle them in existing test rigs. When sticking to CC3, the installation length  $l_i$  of the energy converter can grow up to 130 mm and the installation height  $h_i$  up to 50 mm (spatial directions  $x_2$  and  $x_3$ ). The third direction (spatial direction  $x_1$ ) should be as small as possible.

The necessary force per spatial expansion of the actuator can roughly be 350 N/mm, leading to a force of approx. 45.5 kN for the dimension of 130 mm per side. This gives an idea of the high forces needed for the actuation.

A rough investigation takes place to define the necessary stroke. From an FE-analysis the maximum deformation at the introduction surface of the concrete is determined. At a pressure of 15 MPa with an introduction surface size of  $130\text{ mm} \times 30\text{ mm} = 3900\text{ mm}^2$ , the deformation reaches 0.01 mm in the normal direction. When this deformation is related to the force per spatial extension, a rough value of  $0.0000222\text{ mm}^2/\text{N}$  can be determined, leading to a stroke of roughly 0.0077 mm for the given dimensions and force. Considering this small stroke, it becomes clear that the deformation of the actuator itself will contribute an essential part to the necessary stroke. This part of the stroke depends on the transmission ratio  $i$  of the actuator energy transmission, which considers any leverage effect between the energy converter and the introduction surface, and the yield of the actuator structure. Equation (1) allows a rough calculation of the necessary stroke  $s_{\text{tot}}$ .

$$s_{\text{tot}} = (\delta_{\text{concrete}} + \delta_{\text{structure}}) \cdot F \cdot i \quad (1)$$

with:  $\delta_{\text{concrete}}$ : yield of the concrete, in (mm/N),  $\delta_{\text{structure}}$ : yield of the actuator structure, in (mm/N),  $F$ : applied force, in (N),  $i$ : transmission ratio of the actuator energy transmission.

To calculate the yield of the actuator structure, the Young's modulus, the cross-sectional area, and the length of the structure itself must be known. Potential bending deformations must also be considered.

A necessary stroke of 0.05 mm is assumed for the given basic actuator concepts. A value between 0.05 and 0.1 mm is also used for the design of the energy transmission. In

relation to the dynamics, a quasi-static application of force is assumed for the concepts. The frequency of actuation is, therefore, not particularly relevant.

The actuator itself is planned to be placed directly in the adaptive slab, allowing no option of serviceability. At the current state of research, this is considered sufficient. However, a refined future concept will need to possibly incorporate the option to service the actuator when needed, since the actuator should achieve a lifespan of approximately 50 years or longer. Oil leakage from the actuator must be prevented to avoid contamination of the concrete. For the actuator placed inside slabs within buildings, the hydraulic fluid will experience temperature changes. However, this investigation neglects the effects of fluid dilatation. This is because the type of hydraulic fluid can be freely chosen based on the expected temperature ranges. In real applications, the energy converter will be connected to a controlled hydraulic unit that cancels out the pressure changes caused by fluid dilatation.

Different additional requirements are set when considering CC3 and concrete as the material of the slab. To avoid cracks, the pressure at contact surfaces between the actuator and structural element should not exceed 0.45 times the compressive strength  $f_{ck}$  (cf. [35]) of the concrete used. Sharp edges should also be avoided and the induced forces should mainly be pressure forces. Table 2 gives a rough summary of the requirements for energy converters of actuators for adaptive slabs.

**Table 2.** Excerpt of the identified requirements relating to actuators for adaptive slabs in the scope of Nitzlader et al. [6].

Description	Symbol	Quantity	Unit
Max. stroke in concrete related to force and spatial extension	$s/(F/l)$	0.0000222	$\text{mm}^2/\text{N}$
Max. actuating force per spatial direction related to the spatial extension of the actuator	$F/l$	350	$\text{N}/\text{mm}$
Installation height	$h_i$	45–50	mm
Installation length	$l_i = d_2$	130	mm
Serviceability	-	Not possible	-
Leakage	-	No leakage	-
Max. pressure at contact	$p_{\max}$	$0.45 f_{ck}$	$\text{N}/\text{mm}^2$
Edge condition	-	Rounded	-

### 2.3. Defining Energy Converter Concepts

Comparing the requirements with advantages and disadvantages in [32] and the considerations in [36], hydraulics appear to be an appropriate solution due to their high energy density, long lifetime, and mature technology. The highest energy density can be achieved with hydraulic direct drives. A transmission ratio of one is therefore considered for the energy transmission structure. The value of the force and stroke generated by the energy converter is the final force applied to the structural element.

Systems with static sealings are preferred in order to reduce leakage, canceling out classic piston-cylinder concepts. Hydraulic drives with static sealing are, for example, bellow and membrane (also known as diaphragm) concepts. Due to the small stroke and high complexity of bellow concepts, they are not given further consideration. The membrane concepts appear the most promising. The membranes can feature a flat or corrugated design [37]. The corrugated ones allow a slightly higher stroke. However, additional edges are created inside the concrete and the movement of the membrane could be hindered by concrete inside the grooves. The concepts for this study are therefore limited to flat membranes. Additional processing steps, such as deep forming, are not necessary.

The membranes can be alternated by the connection to the base body of the energy converter and by the material used. Two different materials were chosen:

- Spring steel X10CrNi18-8: high strength, approx. 12% reduced Young's modulus compared to standard steel.

- Polyurethane (PUR) D44 90° Shore A elastomer: highly resistant to abrasion and hydraulic oil, commonly used for sealing.

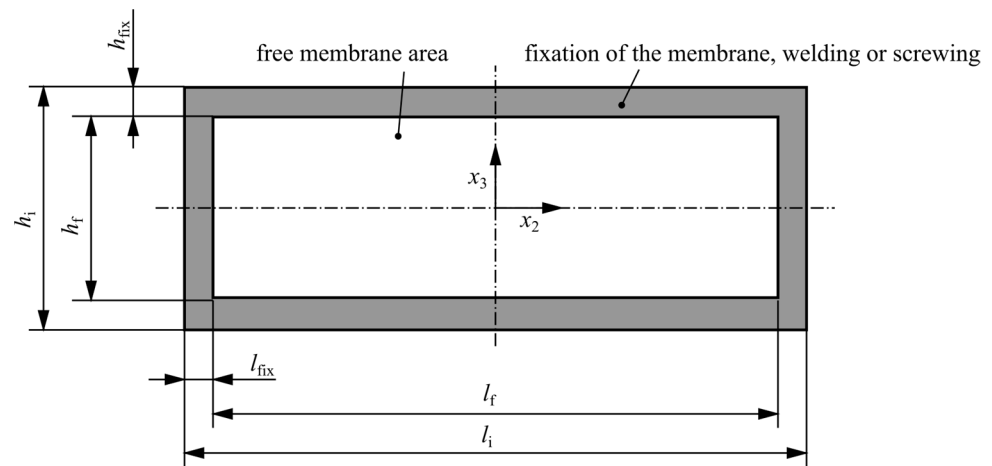
The main objective for the connection to the base body is the greatest possible reduction of construction space in the height of the energy converter, enabling the greatest possible use of 45–50 mm with the free membrane area. This leads to a reduction in the necessary hydraulic pressure. The chosen fixation variants are welding and screwing. Different designs are not feasible due to the higher installation space or insufficient connection strength. The various benefits and disadvantages are listed in Table 3. The free membrane area  $A_f$  is calculated according to Equation (2) and is illustrated in Figure 5.

$$A_f = h_f \cdot l_f \tag{2}$$

with:  $h_f = h_i - 2 \cdot h_{fix}$ : free height of the membrane,  $l_f = l_i - 2 \cdot l_{fix}$ : free length of the membrane,  $h_{fix}$ : height of the fixation, here: 5 mm for welding, 10 mm for screwing,  $l_{fix}$ : length of the fixation, here: 5 mm for welding, 10 mm for screwing.

**Table 3.** Comparison of the connection variants of the membrane to the base body.

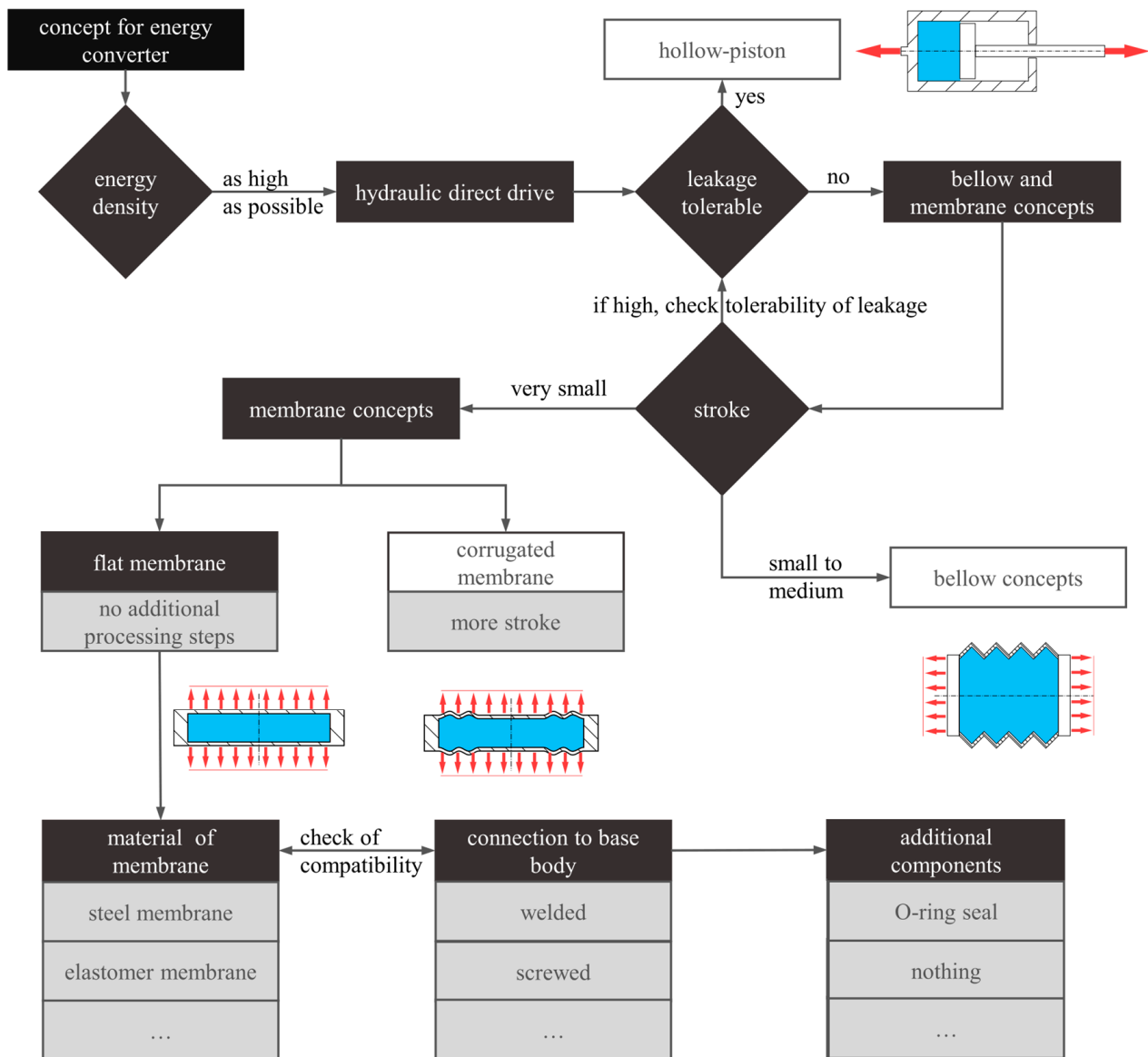
	Screwing	Welding
Pros	<ul style="list-style-type: none"> <li>• Possible for all types of materials, leading to materials with smaller Young’s modulus (e.g., PUR elastomer, metal, ...)</li> <li>• Kind of “overpressure” vent with the seal</li> </ul>	<ul style="list-style-type: none"> <li>• No static or dynamic sealing is necessary</li> <li>• Maximizes the possible free membrane area</li> </ul>
Cons	<ul style="list-style-type: none"> <li>• Additional components necessary</li> <li>• Static seal</li> <li>• Smaller free area of the membrane</li> <li>• Leakage possible</li> </ul>	<ul style="list-style-type: none"> <li>• Possible fatigue in the area of the weld seam, no “overpressure” vent</li> <li>• Only possible for weldable metals</li> </ul>



**Figure 5.** Schematic illustration of the membrane, top view, showing the free membrane area and the area for fixation.

No additional sealing components are necessary for the welded spring steel membrane. Yet, the tightness of the weld seam against hydraulic pressure must be verified. When using the screwed variants, a seal is necessary for the spring steel membrane, while the PUR membrane provides the sealing effect. In the case of the spring steel membrane, a classic elastomer O-ring seal or a metal seal can be used. Metal seals have a significantly longer service life, making them suitable for sealing systems in aerospace applications, while elastomer O-rings are significantly cheaper and their accuracy requirements for the seal

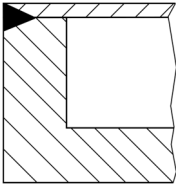
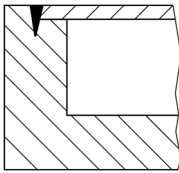
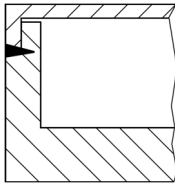
point are lower. O-rings are used as the sealing in the prototype since the service time is not essential in the first investigation. The schematic decision process is shown in Figure 6.



**Figure 6.** Decision process for the energy converter concept, cf. [33]. In the visualizations, blue is the hydraulic fluid with pressure  $p$ , red arrows represent the direction of the force generated by the actuator.

Three concepts for the membrane are considered in terms of the welded variants. The principal concepts are shown in Table 4, combined with a comparison of the advantages and disadvantages of each of the concepts. For the prototype in this investigation, variant one was chosen due to the possibility of in-house manufacturing without bending the steel membrane or using laser welding. For further prototypes, variants two and three are even more promising. The optimal state is assumed with variant 3, in which the area with the highest bending stress does not coincide with the weld seam. This leads to a higher service life.

**Table 4.** Qualitative comparison of different locations for the weld seam. ‘+’ stands for positive, ‘o’ for neutral and ‘–’ for negative points.

Variant 1	Variant 2	Variant 3
		
Heat-conducting seam + Easy manufacturing + No laser welding necessary + No sensitivity to dimensional deviations o Load condition is unclear – Low bond strength – Area of high bending stress coincides with weld seam	Deep weld seam from top + Easy manufacturing + High bond strength o Small sensitivity to dimensional deviations – Laser welding necessary – Area of high bending stress coincides with weld seam	Deep weld seam from the side + Tensile stress at the weld seam + Area of bending does not coincide with weld seam + High bond strength – Additional manufacturing step – Laser welding necessary – High sensitivity to dimensional deviations

With all these considerations, the first basic concepts for the energy converter emerge. Figure 7 shows CAD models of the specimens, while the manufactured specimens are displayed in Figure 8. For variant B, the space for the sealing is manufactured according to the guidelines for the sealing. In variant C, the membrane is compressed with 10% of its thickness.

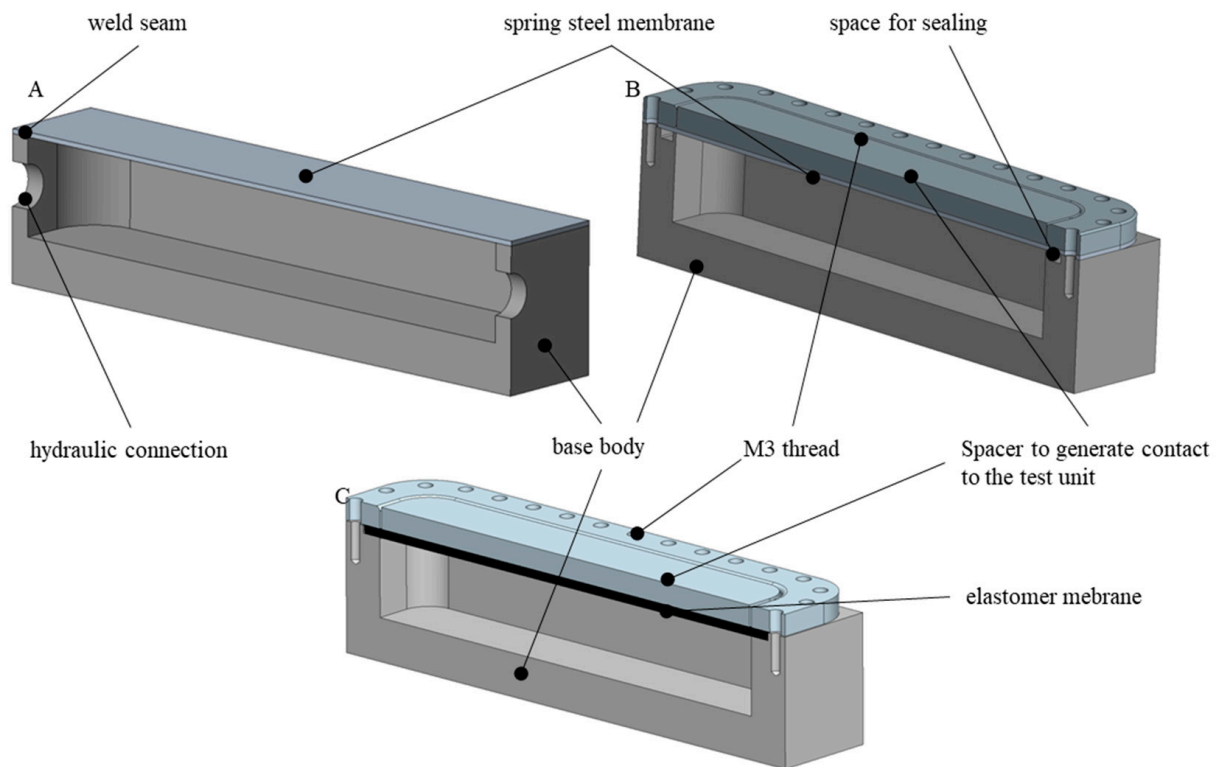


**Figure 7.** CAD model of actuator converter concepts, sectional view. Upper left: welded spring steel (A), upper right: spring steel screwed (B), lower middle: elastomer membrane screwed (C); cf. [33].

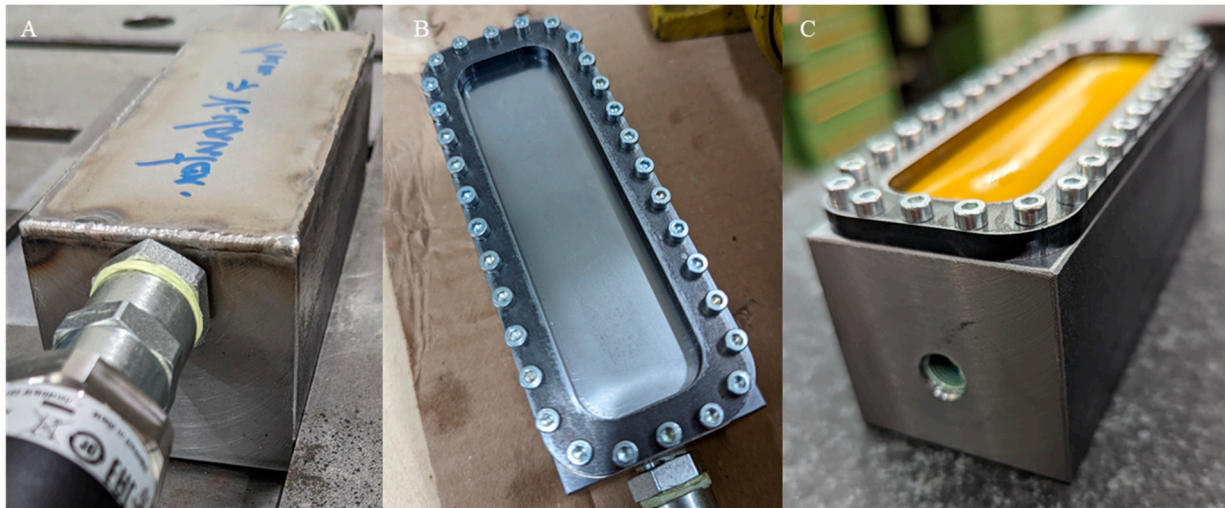


**Figure 8.** Actual prototypes for the different chamber concepts. Left: welded spring steel (A); middle: spring steel screwed (B); right: elastomer membrane screwed (C); spacers for (B,C) not shown; cf. [33].

### 3. Test Setup and Numerical Models

#### 3.1. Test Setup, Test Scenarios, and Evaluation Parameters

The test setup is shown in Figure 9. A tension-compression machine is adapted for the purpose of testing: This makes it possible to record the generated force and stroke in addition to determining the pressure limits of the energy converters. The pressure chamber is vented before a pressure sensor is placed on the venting pipe to avoid air inside the specimen. This results in a closed hydraulic system. Afterward, the pressure is built up with a hydraulic hand pump, while the pressure is measured with the pressure sensor and the force is measured with the load cell of the tension-compression machine.

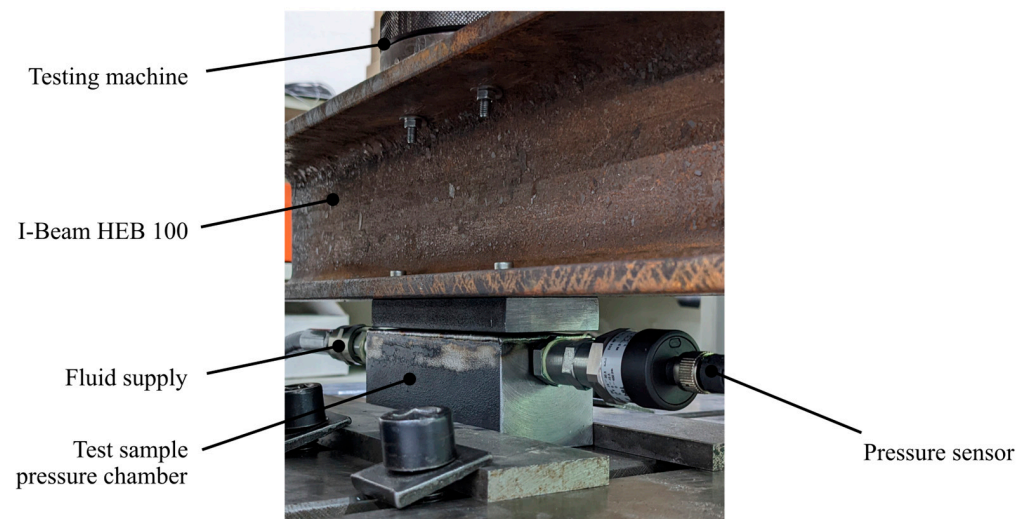


**Figure 9.** Test setup for pressure chambers, cf. [33].

Two different scenarios are used for the test, as shown in Table 5. The evaluation parameters differ between scenarios one and two. In scenario one, the stroke is measured in relation to the pressure at constant force, while in scenario two, the force is measured in relation to the pressure at constant maximum stroke. The force is evaluated in two

parameters to compare the different specimens: a force per free area  $F_f^*$  and a force per installation length  $F_{il}^*$  based on the measurement force  $F_m$ .

$$F_f^* = \frac{F_m}{A_f} \quad (3)$$

$$F_{il}^* = \frac{F_m}{l_i} \quad (4)$$

**Table 5.** Parameters for the test scenarios, cf. [33].

	Scenario 1	Scenario 2
Constant parameter	force	path
Initial condition	defined applied force	defined gap between membrane and loading rig
Force range	1000–5000 N	-
Gap range	-	0–0.05 mm
Pressure limit	2.5 MPa	20 MPa
Evaluation parameter	stroke	force
Tested variants	A	A, B, C

Test scenario one is used for pre-tests optimizing the modeling width of the weld-seam area for variant A, while test scenario two is used for all three variants. In scenario one, the force is limited to 5000 N to avoid damage to the metal membrane in the state without inner pressure. Scenario one is not used for variants B and C to prevent damage to the fixation, to the sealing component in variant B, and to the membrane in variant C. Since the focus is on the reachable forces at a defined maximum stroke, scenario two is more relevant for the prototype validation and the simulations.

### 3.2. Finite Element Models for the Different Prototypes

Different numerical models have been used to model the three specimens. Within the scope of this contribution, elastic and elastic-plastic models are evaluated for the steel membrane, while elastic and hyperelastic models are evaluated for the elastomer membrane. A pre-investigation for comparing two-dimensional and three-dimensional modeling is also conducted.

The material parameters in Table 6 are used for elastic behavior. As an elastic-plastic model, two Ramberg-Osgood curves (cf. [38]) are combined according to [39,40]. Experimental data of a tensile test according to DIN EN ISO 6892 provided by a third party are used to fit the model. For the hyperelastic model of PUR D44, Arruda fitting by ANSYS Workbench is used with data from [41]. The structural steel undergoes linear elastic modeling based on the expectation of low stresses.

**Table 6.** Elastic material parameters for the simulation, cf. [33].

Description	Symbol	Unit	Spring Steel, X10CrNi18-8	Structural Steel, S 235	PUR-Elastomer D44 90° Shore A
Young's modulus	E	N/mm <sup>2</sup>	185,000	210,000	15 (calculated)
Poisson's ratio	$\nu$	-	0.3	0.3	0.48

The pre-investigation is carried out with four different models shown with element types and number of elements in Table 7: A simplified single membrane featuring a fixed bearing on all sides modeled with HEX20 (Figure 10, IV), a single membrane modeled with shell elements (Figure 10, III), a simplified model with symmetries in the y-direction (Figure 10, II), and a two-dimensional model with QUAD8 (Figure 10, I). The sizes of the elements are set in a way to ensure accurate modeling of the contact surface with neighboring components in later models of the entire energy converter. Here, the fixation area is

neglected, increasing the free membrane area to the installation length  $l_i$  and installation height  $h_i$ .

**Table 7.** Element type and number of elements and nodes for the different models in the pre-investigation.

Description	I	II	III	IV
Element type	QUAD8	HEX20	SHELL181	HEX20
Number of nodes	821	45,261	22,320	285,281
Number of elements	250	10,000	21,988	65,000

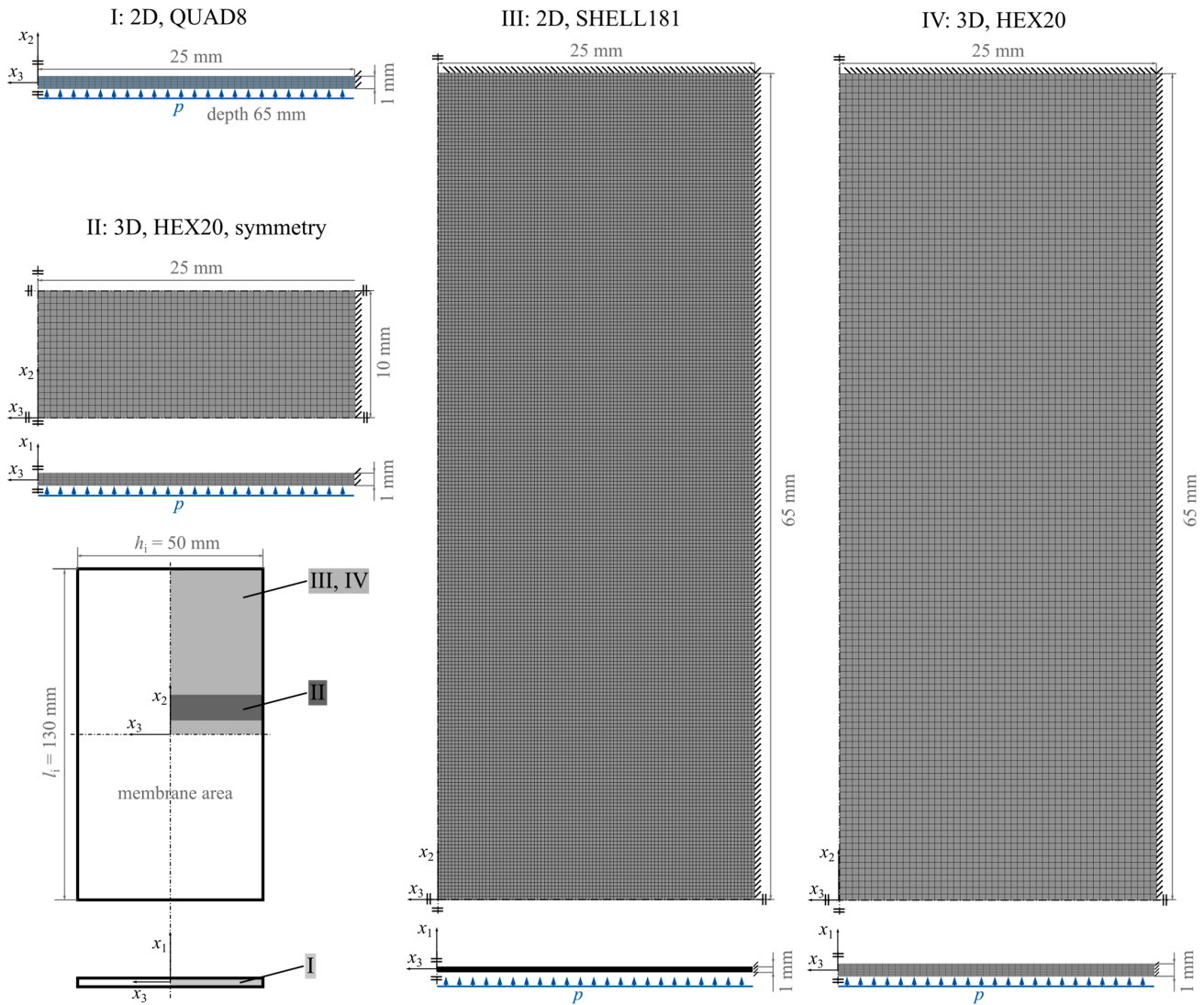


**Figure 10.** FE models for comparison of 3D and 2D modeling and material models, also the boundary conditions are visible, subfigure I is the 2D model with QUAD8 elements and with symmetry in  $x_3$ -direction, subfigure II is the 3D-model with HEX20 elements and with symmetries in  $x_2$ - and  $x_3$ -direction, subfigure III is the 3D model with SHELL181 elements and with symmetry in  $x_1$ -,  $x_2$ - and  $x_3$ -direction, subfigure IV is the 3D model with HEX20 elements and with symmetry in  $x_2$ - and  $x_3$ -direction.

The same models are used to compare the material behavior. In the later stage, more detailed models are used to depict the experimental setup. Therefore, the loading rig is also modeled to a certain point to account for its small deformations. A two-dimensional approach is used for the welded variants, as shown in Figure 11. The experimental data

of scenario one are used to tune the model. Here, the welded area length is adapted so that the experiment and simulation results fit relatively well, as shown in the following chapter. A 3D model is subsequently used to compare the results and perform a parameter variation for rotational deviations.

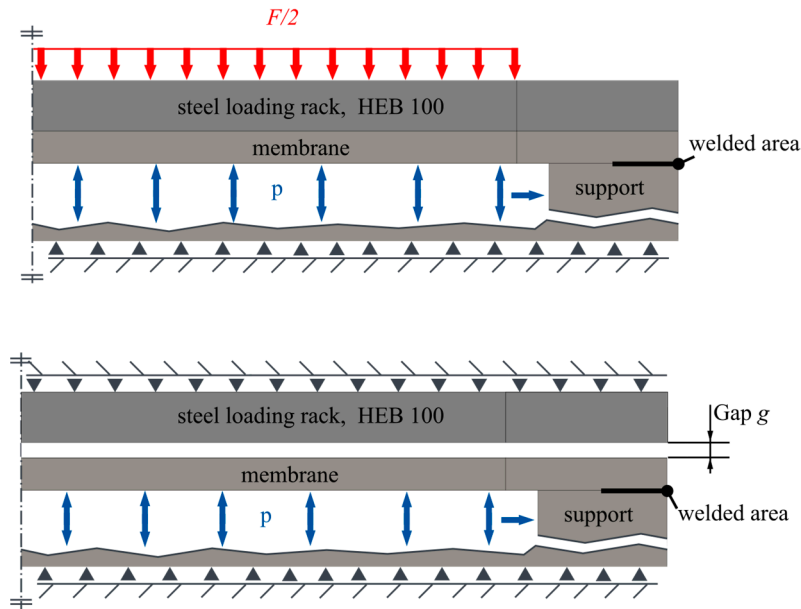


**Figure 11.** FE model for the welded chambers (top: force controlled/scenario one; bottom: path controlled/scenario two). The applied hydraulic pressure  $p$  is given with blue arrows, in red is the testing force  $F$ , and the triangles mark the fixed boundary conditions.

A three-dimensional section with symmetries in three directions is modeled for the screwed models. The clamping of the membrane with bolts can be included in the model. The maximum pre-tensioning force used is that of an M3 screw with strength classification 10.9. Figure 12 depicts the models and Table 8 shows the number of elements for the different models.

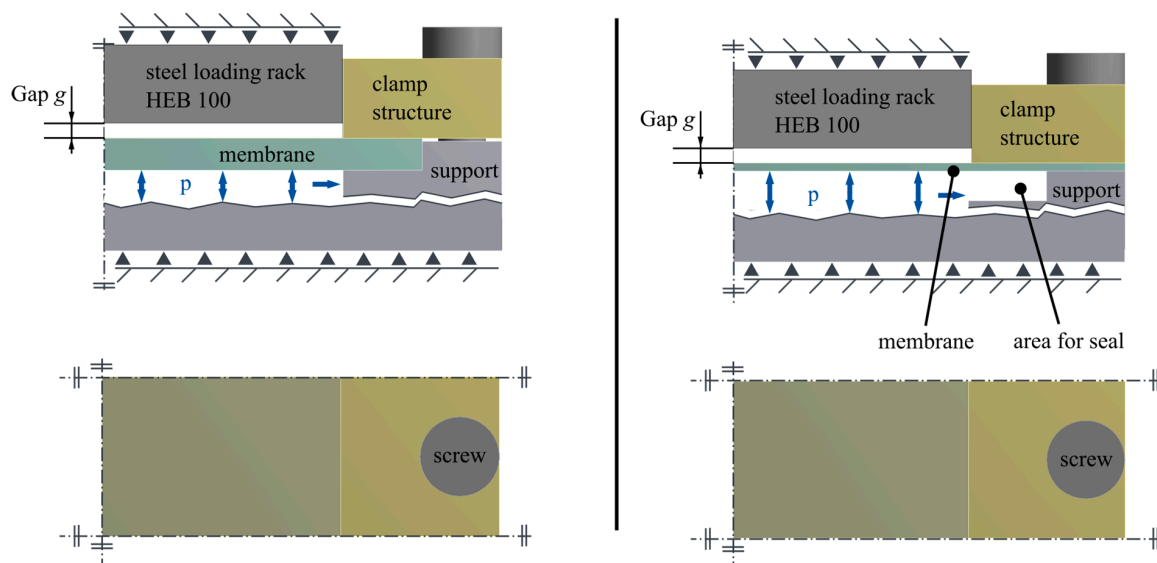


**Figure 12.** FE model for the screwed chambers. Left: elastomer membrane; right: spring steel membrane, used for scenario two. The applied hydraulic pressure  $p$  is given with blue arrows and the triangles mark the fixed boundary conditions.

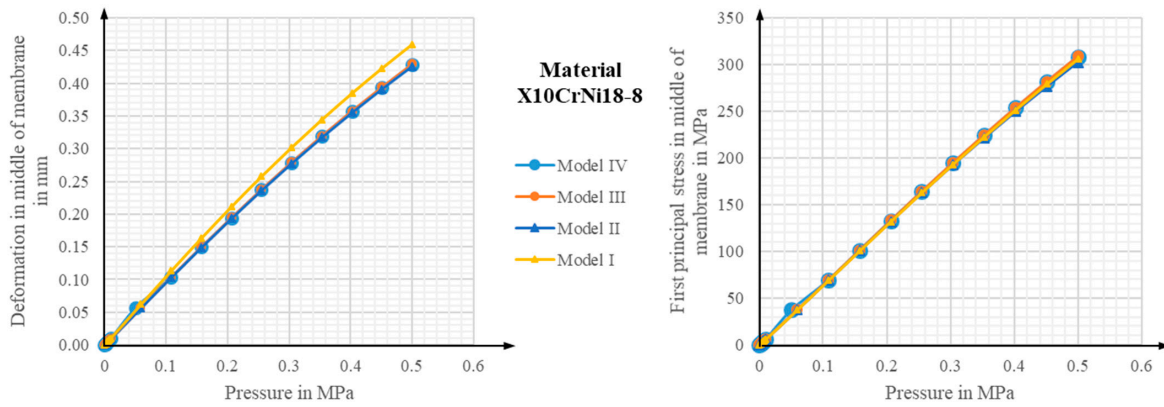
**Table 8.** Number of elements and nodes for the different models for the primary investigation.

Description	Welded, 2D	Welded, 3D	Screwed, 3D Metal	Screwed, 3D Elastomer
Nodes	214,516	350,010	527,991	527,991
Elements	70,096	179,637	274,176	274,176

## 4. Results

### 4.1. Comparison of Two- and Three-Dimensional Finite Element Basic Models

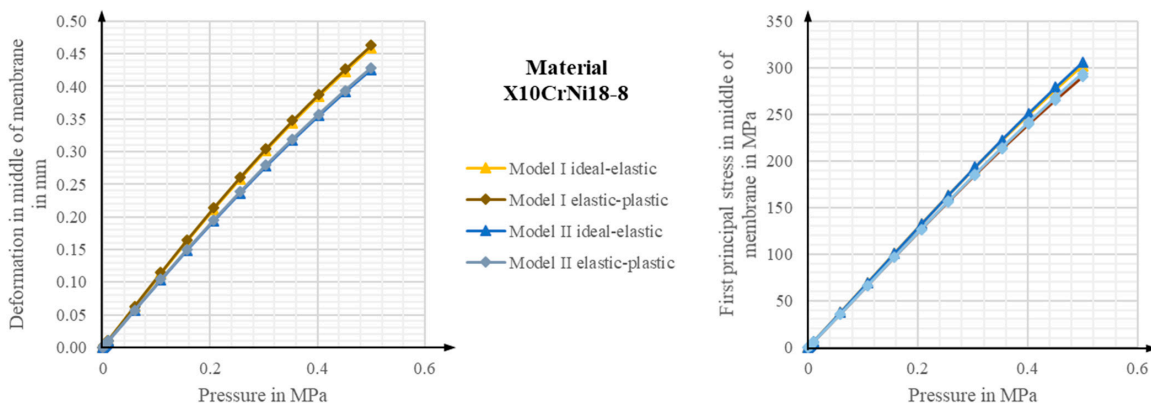
This investigation analyzes both the maximum deflection and the maximum first principal stress in the middle of the membrane. As shown in Figure 13, the results fit relatively well for the different models I, II, III, and IV. The 2D model (model I) has a slightly larger deformation. All stresses are within the same range. Due to the much shorter calculation time, the concept of model I is used for the welded variants. In the case of the screwed variants, the concept of model II is used. The models will be used for the subsequent design of actuators with different membrane lengths and heights in order to generate a rough estimate of the attainable forces and strokes for the various stresses.



**Figure 13.** Comparison of the deformation and first principal stresses in middle of membrane based on different models for spring steel X10CrNi18-8.

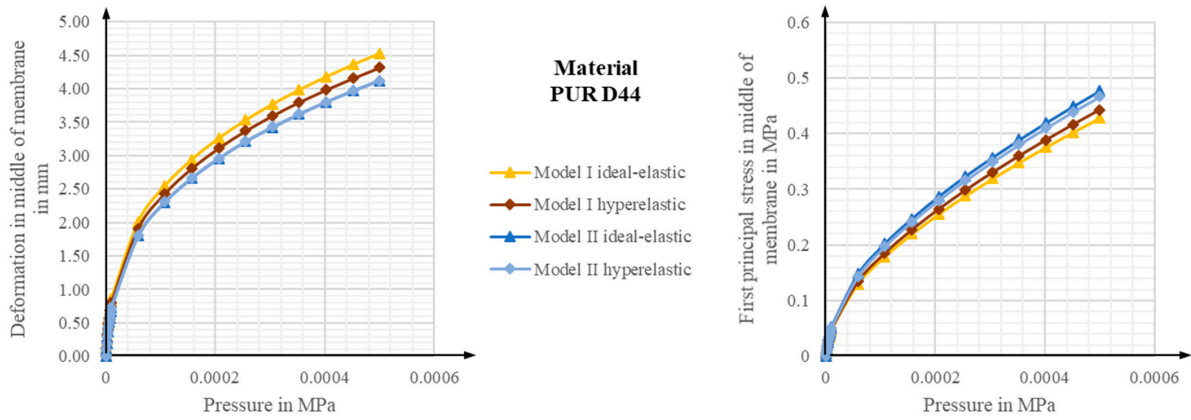
### 4.2. Comparison of Elastic, Elastic-Plastic, and Hyperelastic Models

Figure 13 depicts the maximum deflection for the spring steel in terms of an elastic and an elastic-plastic model. Slightly higher values are generated for the deflection of the elastic-plastic models. The stress in the middle of the membrane is also reduced by around 4%, as shown in Figure 14. This could be caused by small moments of plastification.



**Figure 14.** Comparison of the deformation and first principal stresses in middle of membrane based on different material models for spring steel X10CrNi18-8.

In the case of the elastomer, the pressure was reduced to a maximum of 0.005 MPa due to the lower material stiffness. Similar levels of deflection and stress were recorded for both models (cf. Figure 15) with a deviation of around 5%.



**Figure 15.** Comparison of the deformation and first principal stresses in middle of membrane based on different material models for elastomer PUR D44.

The linear elastic model is used for further investigation, giving a rough estimate of the expected stresses and deformation. The stability of the models is higher, and results can be achieved more quickly.

#### 4.3. Model Tuning with Scenario One

Figure 16 shows the results of the measurements for scenario one, along with a simulation featuring an optimized weld seam area. The depth of the weld seam was the main parameter for the simulation output in this context and was detected accordingly. The data shown in Figure 16 have been generated with values for the bonded contact of 50% of the connection surface. The pressure increase in the experiment was stopped at a stroke of around 0.5 mm to avoid damage to the specimen. No leakage or damage was visible following this test, although minor plastic deformation of the membrane was observed. The initial exponential behavior of the stroke is visible before transforming into a linear dependence. This may be caused by the deformation of the membrane. The visible gap between the experimental and numerical data may be caused by effects that were not accounted for, such as a lack of perfectly tuned weld seam length, lack of ideal bonded behavior of the weld seam in reality, or deviations along the length of the weld seam due to manufacturing restrictions.

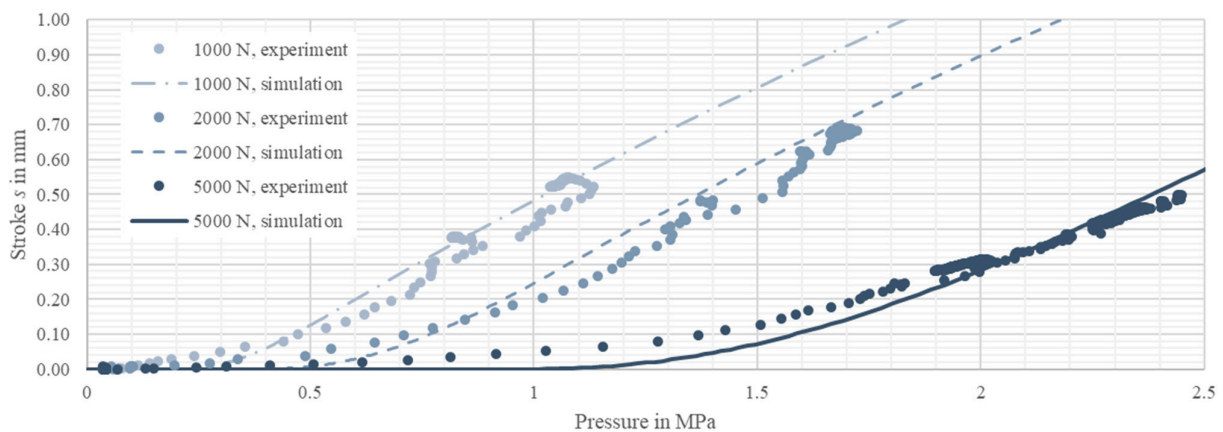


**Figure 16.** Measurement data for scenario one, variant A (heat-conducting seam), with experimental and simulation data in scenario one; cf. [33].

#### 4.4. Experimental Results for Scenario Two

For scenario two, the forces per free area plotted against the pressure are shown in Figure 17. It is visible that the steel membranes behave in a similar range for all variants. The elastomer variants raised them to a pressure of 10 MPa. At this point, leakage occurred, and the force could not be increased further. The welded variant demonstrated leakage in a later test at a pressure above 20 MPa, which is not shown in the diagrams. Minor leakage also occurred at a pressure above 20 MPa for the variants with the O-ring.

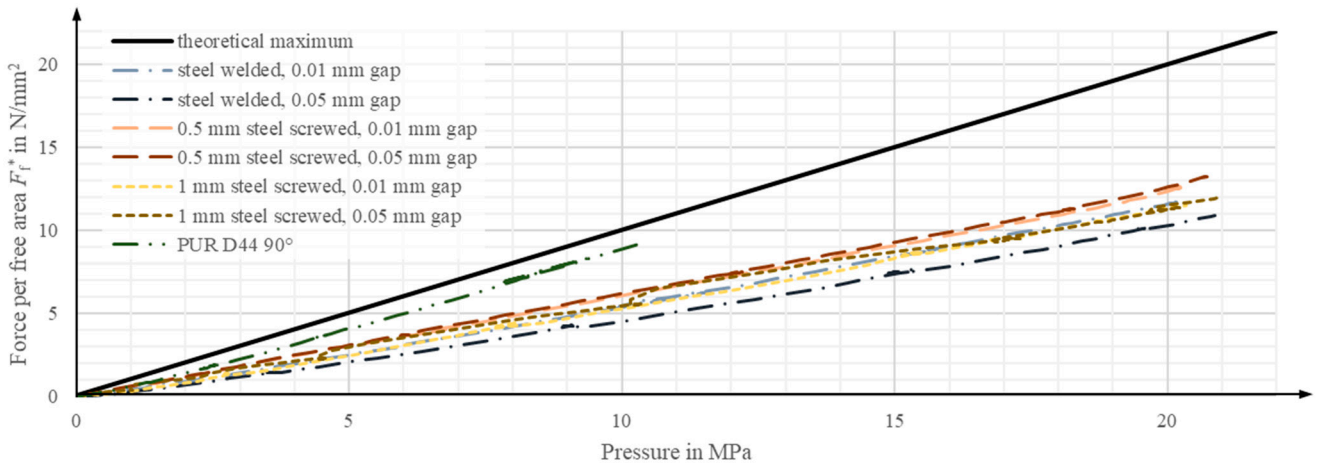


**Figure 17.** Measurement data related to free membrane area for different membrane types and defined strokes in scenario two, cf. [33].

When using the criterion of force per installation length, as shown in Figure 18, the welded variants reach the required value of 350 N/mm at a pressure of about 17 MPa, depending on the initial gap. The screwed variants do not reach that value within 20 MPa. In the case of the elastomer, an optimized version with leakage at a higher pressure level could be promising as its force value is above the welded variants up to the leakage point of 10 MPa. This is ensured by the lower Young’s modulus, meaning that less force is necessary for the deformation of the membrane.

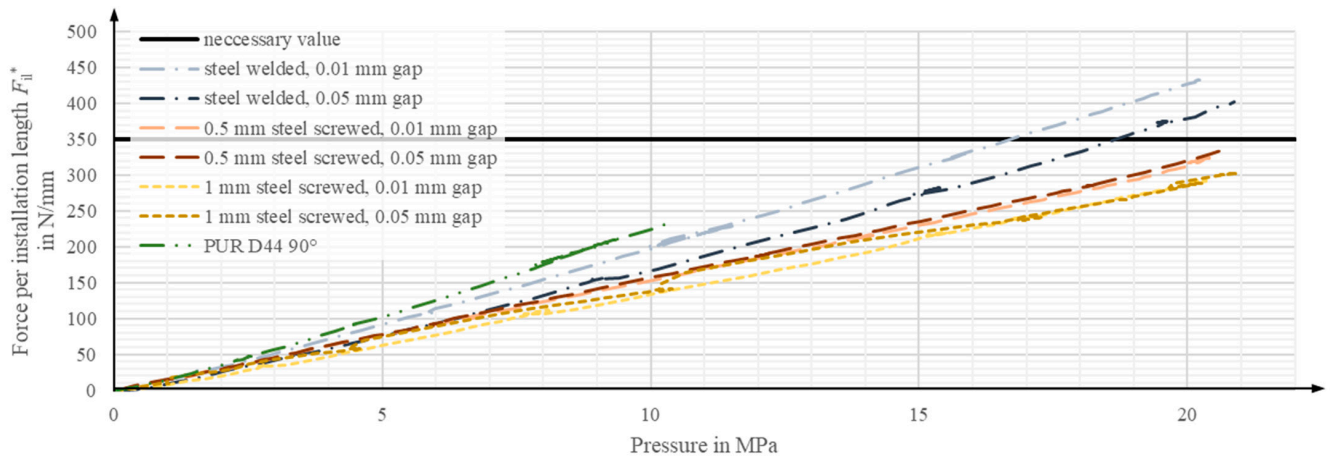


**Figure 18.** Measurement data related to installation area for different membrane types and defined strokes in scenario two, cf. [33].

#### 4.5. Comparison of Numerical and Experimental Results

When comparing the numerical and experimental results, as in Figure 19, the picture is mixed. In the simulation, the force per free membrane area is overestimated by a factor of 1.45 for the metal membrane variants. For the elastomer membrane, the gap is significantly

smaller. The grading between the different variants is the same for the experiment and the simulation. An additional comparison with a 3D-modeled welded model has been carried out to achieve better results and has recorded similar values for the force (see Figure 20). The simulation shows a higher potential for the achievable forces than was measured in the experiments. The staging of the forces for the different actuator chamber prototypes is consistent for experiment and simulation.

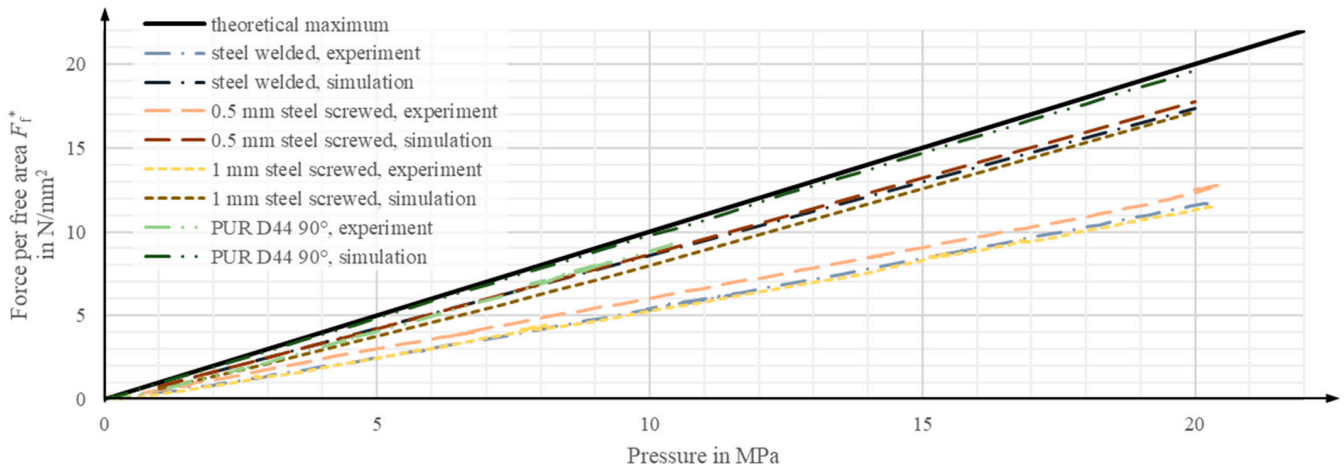


**Figure 19.** Measurement data and simulation data related to free membrane area for different membrane types at a defined stroke of 0.05 mm in scenario two, cf. [33].

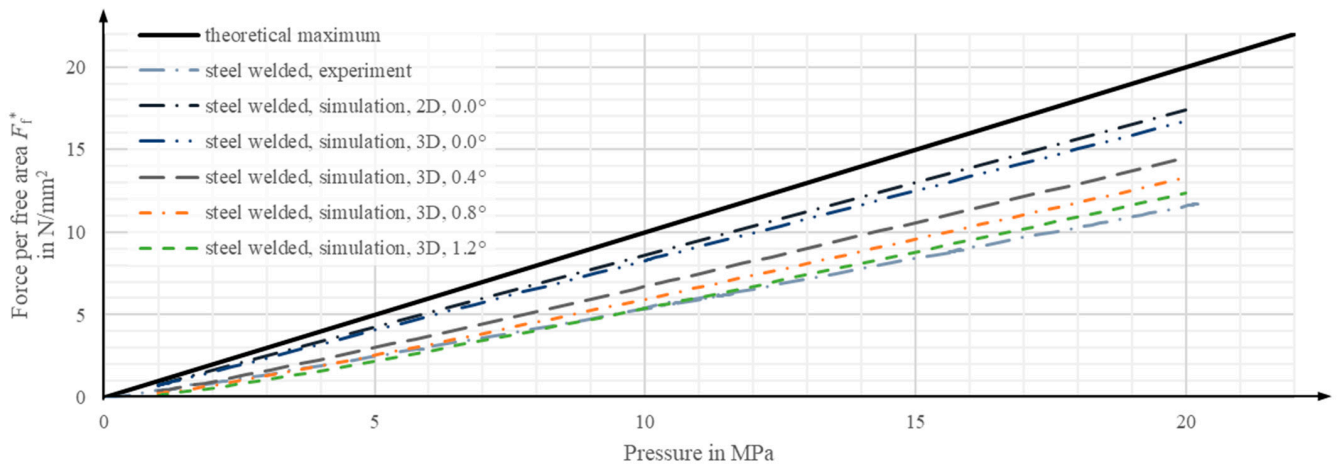


**Figure 20.** Results of the parameter study for rotational deviation for a steel membrane at a defined stroke of 0.05 mm in scenario two.

#### 4.6. Influence of Slight Rotational Deviations on the Experiment Results

An investigation of the influence of rotational deviations in the test setup was performed to increase the accuracy of the simulations. A 3D-half model of the welded variant was therefore used. The fluid chamber was rotated around the longitudinal axis in increments of 0 to 1.2°, with the results shown in Figure 20. It can be observed that the force drops significantly even in the context of slight deviations, leading to the conclusion that higher force values appear to be feasible in ideal conditions.

## 5. Discussion

The designed concepts for energy converters for integrated actuators in slabs can be experimentally validated according to the identified requirements. Thus, the assumptions and the design process seem to be feasible. In addition, the simplified numerical models

can be used for a first rough estimation of how an actuator will behave in terms of forces when a particular design space is specified.

The necessary force per installation length  $F_{il}$  of 350 N/mm is achieved with the welded membrane variants at a pressure of approximately 17 MPa. The required stroke of 0.05 mm is also achieved. However, the elastomer membranes can achieve the highest efficiency as well as the required stroke due to the minimal energy required to deform the membrane in the given design space, but cannot reach the 350 N/mm value due to leakage at 10 MPa with the current design. When going further in the next evolution step, the leakage at 10 MPa could be prevented by increasing the compression at the sealing points or changing the geometry. Additional simulations, therefore, need to be carried out. As a reference, the observed leakage at around 10 MPa can be used to validate the models. The potential for higher strokes than 0.05 mm is also given due to the lower stiffness of the material compared to the steel membranes. An acceptable result can be observed for the bolted steel membranes, but the generated force per installation length is significantly lower than the welded variants and does not reach the required value force up to 20 MPa hydraulic pressure. The welded and elastomeric variants should be further considered for the next evolutionary steps. In the simulation models, the stresses in the weld seam reach relatively high values. This is also consistent with the leakage observed in the welded variants at pressures higher than 20 MPa. The proposed improved designs could be used for the next steps. Switching the technology from hand welding to laser welding could also further improve the quality of the weld. This makes it possible to achieve a deep weld that reaches a higher strength limit.

Simplification of the models to 2D (welded) and 3D with symmetry (bolted) was also verified and validated with the experimental results. These models can be used to estimate how an actuator will behave in terms of forces and strokes for a given design space. The gap observed between numerical and experimental results could be caused by underestimating the stiffness or deformations within the test rig that have not yet been considered. As shown, slight rotational deviations in the test setup cause a significant change in the forces that can be achieved, leading to the conclusion that the rotational position should be more precise in further experiments. The whole test unit could also be modeled in this context. Nevertheless, the results can be used for further investigations if the membrane height is similar. The results provide an initial outlook on the potential of the concepts, with the simulations showing even greater potential for the forces that can be achieved.

## 6. Conclusions

Specialized actuators are necessary to achieve maximum resource savings for adaptive two-way slabs. The energy converter is an essential component of the actuators. The paper outlines a decision process for energy converter concepts, comparing the individual parts of the actuators, as well as a simplified simulation strategy. The experimental comparison of different membrane materials with their respective mounting solutions revealed that the elastomer membrane can generate the highest forces in relation to the necessary hydraulic pressure in a small installation space. In contrast, the steel membrane can achieve the necessary absolute force due to its ability to withstand higher pressure. The finite element simulations performed show good agreement with the experimental results, even with the modeling simplifications applied. Essential parts for a good agreement between simulation and experiment, such as rotational deviations, could be identified by varying individual modeling parameters. In addition, identified drawbacks, such as the leakage of the elastomer membrane above 10 MPa, can be taken into account in future simulations to optimize, e.g., the pretension of the elastomer. This means that decisions on the choice of energy converter concept can be made more efficiently in the future, even without the support of experimental tests.

**Author Contributions:** Conceptualization, M.J.B. and M.N.; methodology, M.J.B.; software, M.J.B.; validation, M.J.B.; formal analysis, M.J.B.; investigation, M.J.B. and M.N.; resources, M.J.B.; data curation, M.J.B.; writing—original draft preparation, M.J.B.; writing—review and editing, M.J.B.,

M.N., M.B., H.B., L.B. and M.K.; visualization, M.J.B.; supervision, M.B., L.B., H.B. and M.K.; project administration, L.B., H.B. and M.K.; funding acquisition, L.B., H.B. and M.K. All authors have read and agreed to the published version of the manuscript.

**Funding:** This work is funded by the Deutsche Forschungsgemeinschaft (DFG, German Research Foundation)—project ID 279064222—SFB 1244. The authors are grateful for the generous support.

**Data Availability Statement:** Most of the data presented in this study are available on request from the corresponding author. Some data were obtained from a third party.

**Conflicts of Interest:** The authors declare no conflict of interest.

## References

1. UNEP. *Status Report for Buildings and Construction: Towards a Zero-Emission, Efficient and Resilient Buildings and Construction Sector*; UNEP: Nairobi, Kenya, 2020.
2. Sobek, W. Ultra-lightweight construction. *Int. J. Space Struct.* **2016**, *31*, 74–80. [[CrossRef](#)]
3. Wang, Y.; Senatore, G. Design of adaptive structures through energy minimization: Extension to tensegrity. *Struct. Multidiscipl. Optim.* **2021**, *64*, 1079–1110. [[CrossRef](#)] [[PubMed](#)]
4. Ostertag, A.; Dazer, M.; Bertsche, B.; Schlegl, F.; Albrecht, S.; Leistner, P.; Gienger, A.; Wagner, J.; Tarin, C.; Sawodny, O. Reliable Design of Adaptive Load-Bearing Structures with Focus on Sustainability. In Proceedings of the 30th European Safety and Reliability Conference and 15th Probabilistic Safety Assessment and Management Conference, (ESREL), Venice, Italy, 1–5 November 2020; Baraldi, P., Di Maio, F., Zio, E., Eds.; Research Publishing Services: Singapore, 2020; pp. 4703–4710, ISBN 978-981-14-8593-0. [[CrossRef](#)]
5. Burghardt, T.; Kelleter, C.; Bosch, M.; Nitzlader, M.; Bachmann, M.; Binz, H.; Blandini, L.; Sobek, W. Investigation of a large-scale adaptive concrete beam with integrated fluidic actuators. *Civ. Eng. Des.* **2022**, *4*, 35–42. [[CrossRef](#)]
6. Nitzlader, M.; Steffen, S.; Bosch, M.J.; Binz, H.; Kreimeyer, M.; Blandini, L. Designing Actuation Concepts for Adaptive Slabs with Integrated Fluidic Actuators Using Influence Matrices. *CivilEng* **2022**, *3*, 809–830. [[CrossRef](#)]
7. Berger, T.; Prasser, P.; Reinke, H.G. Einsparung von Grauer Energie bei Hochhäusern. *Beton-Und Stahlbetonbau* **2013**, *108*, 395–403. [[CrossRef](#)]
8. Flatt, R.J.; Roussel, N.; Cheeseman, C.R. Concrete: An eco material that needs to be improved. *J. Eur. Ceram. Soc.* **2012**, *32*, 2787–2798. [[CrossRef](#)]
9. Janocha, H. *Actuators: Basics and Applications; with 47 Tables*; Springer: Berlin/Heidelberg, Germany, 2004; ISBN 978-3-642-08266-5. [[CrossRef](#)]
10. Isermann, R. *Mechatronische Systeme: Grundlagen, 2. Neu Bearb. Aufl. 2008*; Springer: Berlin/Heidelberg, Germany, 2008; ISBN 978-3-540-32512-3.
11. Czichos, H. *Mechatronik*; Springer Fachmedien Wiesbaden: Wiesbaden, Germany, 2019; ISBN 978-3-658-26293-8. [[CrossRef](#)]
12. Soong, T.T.; Manolis, G.D. Active Structures. *J. Struct. Eng.* **1987**, *113*, 2290–2302. [[CrossRef](#)]
13. Blandini, L.; Haase, W.; Weidner, S.; Böhm, M.; Burghardt, T.; Roth, D.J.; Sawodny, O.; Sobek, W. D1244: Design and construction of the first adaptive high-rise experimental building. *Front. Built Environ.* **2022**, *8*, 814911. [[CrossRef](#)]
14. Schnellenbach-Held, M.; Fakhouri, A.; Steiner, D.; Kühn, O. *Adaptive Spannbetonstruktur Mit lernfähigem Fuzzy-Regelungssystem*; Carl Schünemann Verlag: Bremen, Germany, 2014; ISBN 978-3-95606-084-7.
15. Neuhaeuser, S.; Weickgenannt, M.; Witte, C.; Haase, W.; Sawodny, O.; Sobek, W. Stuttgart smartshell—A full scale prototype of an adaptive shell structure. *J. Int. Assoc. Shell Spat. Struct.* **2013**, *54*, 259–270.
16. Steffen, S.; Nitzlader, M.; Burghardt, T.; Binz, H.; Blandini, L.; Sobek, W. An Actuator Concept for Adaptive Concrete Columns. *Actuators* **2021**, *10*, 273. [[CrossRef](#)]
17. Senatore, G.; Duffour, P.; Winslow, P. Synthesis of minimum energy adaptive structures. *Struct. Multidisc. Optim.* **2019**, *60*, 849–877. [[CrossRef](#)]
18. Rekswardojo, A.P.; Senatore, G. Design of ultra-lightweight and energy-efficient civil structures through shape morphing. *Comput. Struct.* **2023**, *289*, 107149. [[CrossRef](#)]
19. Senatore, G.; Duffour, P.; Winslow, P.; Wise, C. Shape control and whole-life energy assessment of an ‘infinitely stiff’ prototype adaptive structure. *Smart Mater. Struct.* **2018**, *27*, 15022. [[CrossRef](#)]
20. Rekswardojo, A.P.; Senatore, G.; Srivastava, A.; Carroll, C.; Smith, I.F. Design and testing of a low-energy and -carbon prototype structure that adapts to loading through shape morphing. *Int. J. Solids Struct.* **2022**, *252*, 111629. [[CrossRef](#)]
21. Soong, T.T.; Masri, S.F.; Housner, G.W. An Overview of Active Structural Control under Seismic Loads. *Earthq. Spectra* **1991**, *7*, 483–505. [[CrossRef](#)]
22. Abdel-Rohman, M.; Leipholz, H.H. Active Control of Tall Buildings. *J. Struct. Eng.* **1983**, *109*, 628–645. [[CrossRef](#)]
23. Reinhorn, A.M.; Soong, T.T.; Lin, R.C.; Riley, M.A.; Wang, Y.P.; Aizawa, S.; Higashino, M. *Active Bracing System: A Full Scale Implementation of Active Control, Technical Report NCEER-92-0020, 1992*; National Center for Earthquake Engineering Research, University at Buffalo: New York, NY, USA, 1992. [[CrossRef](#)]
24. Bani-Hani, K.; Ghaboussi, J. Nonlinear Structural Control Using Neural Networks. *J. Eng. Mech.* **1998**, *124*, 319–327. [[CrossRef](#)]

25. Connor, J.J. *Introduction to Structural Motion Control*; Prentice Hall: Upper Saddle River, NJ, USA, 2003; ISBN 0130091383.
26. Heidenreich, C. Adaptivität von Freigeformten Flächentragwerken-Möglichkeiten zur Steigerung der Effizienz von Faserverbundstrukturen im Bauwesen. Ph.D. Thesis, Bauhaus-Universität Weimar, Weimar, Germany, 2016. [[CrossRef](#)]
27. Trautwein, A.; Prokosch, T.; Bischoff, M. A case study on tailoring stiffness for the design of adaptive rib-stiffened slabs. In *Towards White-Box Modeling of Sensory-Utilized Rolling Bearings, Proceedings of the 10th ECCOMAS Thematic Conference on Smart Structures and Materials, Patras, Greece, 7 March–7 May 2023*; Puchtlar, S., van der Kuip, J., Kirchner, E., Eds.; Department of Mechanical Engineering & Aeronautics, University of Patras: Patras, Greece, 2023; pp. 671–678, ISBN 978-960-88104-6-4. [[CrossRef](#)]
28. Korvink, J.-G.; Schlaich, M. Autonome Brücken-ein Blick in die ferne Zukunft des Brückenbaus. *Bauingenieur* **2000**, *75*, 29–34.
29. Bossens, F.; Preumont, A. Active tendon control of cable-stayed bridges: A large-scale demonstration. *Earthq. Eng. Struct. Dyn.* **2001**, *30*, 961–979. [[CrossRef](#)]
30. Weilandt, A. Adaptivität bei Flächentragwerken. Ph.D. Thesis, Universität Stuttgart, Stuttgart, Germany, 2008. [[CrossRef](#)]
31. Marker, P.; Bleicher, A. A Hierarchical Optimization Method for the Design of Active Hybrid Structures. *Front. Built Environ.* **2022**, *8*, 705434. [[CrossRef](#)]
32. Kelleter, C. Untersuchungen Zur Manipulation Des Lastabtrages Biegebeanspruchter Betonbauteile Durch Integrierte Fluidische Aktoren. Ph.D. Thesis, Universität Stuttgart, Stuttgart, Germany, 2022. [[CrossRef](#)]
33. Bosch, M.J.; Nitzlader, M.; Bachmann, M.; Binz, H.; Blandini, L.; Kreimeyer, M. Experimental Testing of Actuator Chambers of Integrated Fluidic Actuators for Adaptive Slabs. In *Proceedings of the ICEM20, Experimental Mechanics in Engineering and Biomechanics, Porto, Portugal, 2–7 June 2023*; Silva Gomes, J.F., Ed.; INEG: Porto, Portugal, 2023; ISBN 978-989-54756-7-4.
34. Bosch, M.; Nitzlader, M.; Burghardt, T.; Bachmann, M.; Binz, H.; Blandini, L.; Kreimeyer, M. Design of integrated fluidic actuators for multi-axial loaded structural elements. In *Proceedings of the 8th European Congress on Computational Methods in Applied Sciences and Engineering, CIMNE, Oslo, Norway, 5–9 June 2022*. [[CrossRef](#)]
35. DIN Deutsches Institut für Normung e., V. *DIN EN 206, Concrete-Specification, Performance, Production and Conformity, German Version EN 206:2013+A2:2021*; Beuth Verlag GmbH: Berlin, Germany, 2021.
36. Weidner, S.; Kelleter, C.; Sternberg, P.; Haase, W.; Geiger, F.; Burghardt, T.; Honold, C.; Wagner, J.; Böhm, M.; Bischoff, M.; et al. The implementation of adaptive elements into an experimental high-rise building. *Steel Constr.* **2018**, *11*, 109–117. [[CrossRef](#)]
37. Di Giovanni, M. *Flat and Corrugate Diaphragm Design Handbook*; Dekker: New York, NY, USA, 1982; ISBN 0824712811.
38. Ramberg, W.; Osgood, W.R. Description of Stress-Strain Curves by Three Parameters NACA-TN-902. 1943. Available online: <https://ntrs.nasa.gov/citations/19930081614> (accessed on 7 December 2023).
39. Li, T.; Zheng, J.; Chen, Z. Description of full-range strain hardening behavior of steels. *Springerplus* **2016**, *5*, 1316. [[CrossRef](#)] [[PubMed](#)]
40. Falter, J.; Binz, H.; Kreimeyer, M. Investigations on design limits and improved material utilization of press-fit connections using elastic-plastic design. *Appl. Eng. Sci.* **2023**, *13*, 100124. [[CrossRef](#)]
41. Junik, K.; Lesiuk, G.; Duda, S.; Jamroziak, K.; Błażejowski, W.; Zielonka, P.; Socha, T.; Denisiewicz, A.; Kula, K.; Szczurek, A. Constitutive Law Identification and Fatigue Characterization of Rigid PUR Elastomers 80 ShA and 90 ShA. *Materials* **2022**, *15*, 6745. [[CrossRef](#)] [[PubMed](#)]

**Disclaimer/Publisher’s Note:** The statements, opinions and data contained in all publications are solely those of the individual author(s) and contributor(s) and not of MDPI and/or the editor(s). MDPI and/or the editor(s) disclaim responsibility for any injury to people or property resulting from any ideas, methods, instructions or products referred to in the content.